Research Article | Vol. 9, No. 5 | 1 May 2018 | BIOMEDICAL OPTICS EXPRESS 2383

Biomedical Optics EXPRESS

Intravital imaging of a pulmonary endothelial surface layer in a murine sepsis model

INWON PARK,[1] KIBAEK CHOE,[2,3] HOWON SEO,[2,3] YOONHA HWANG,[2,3] EUNJOO SONG,[2,3] JINHYO AHN,[2,3] YOU HWAN JO,[4,5,6] AND PILHAN KIM[1,2,3,7]

[1]*Graduate School of Medical Science and Engineering, Korea Advanced Institute of Science and Technology (KAIST), 291 Daehak-ro, Yuseong-gu, Daejeon, 34141, South Korea*
[2]*Graduate School of Nanoscience and Technology, Korea Advanced Institute of Science and Technology (KAIST), 291 Daehak-ro, Yuseong-gu, Daejeon, 34141, South Korea*
[3]*KI for Health Science and Technology (KIHST), Korea Advanced Institute of Science and Technology (KAIST), 291 Daehak-ro, Yuseong-gu, Daejeon, 34141, South Korea*
[4]*Department of Emergency Medicine, Seoul National University Bundang Hospital (SNUBH), 82 Gumi-ro, 173 Beon-gil, Bundang-gu, Seongnam-si, Gyeonggi-do, 13620*
[5]*Department of Emergency Medicine, Seoul National University College of Medicine (SNUCM), 103 Daehak-ro, Jongno-gu, Seoul, 03080, South Korea*
[6]*emdrjyh@gmail.com*
[7]*pilhan.kim@kaist.ac.kr*

Abstract: Direct intravital imaging of an endothelial surface layer (ESL) in pulmonary microcirculation could be a valuable approach to investigate the role of a vascular endothelial barrier in various pathological conditions. Despite its importance as a marker of endothelial cell damage and impairment of the vascular system, *in vivo* visualization of ESL has remained a challenging technical issue. In this work, we implemented a pulmonary microcirculation imaging system integrated to a custom-design video-rate laser scanning confocal microscopy platform. Using the system, a real-time cellular-level microscopic imaging of the lung was successfully performed, which facilitated a clear identification of individual flowing erythrocytes in pulmonary capillaries. Subcellular level pulmonary ESL was identified *in vivo* by fluorescence angiography using a dextran conjugated fluorophore to label blood plasma and the red blood cell (RBC) exclusion imaging analysis. Degradation of ESL width was directly evaluated in a murine sepsis model *in vivo*, suggesting an impairment of pulmonary vascular endothelium and endothelial barrier dysfunction.

© 2018 Optical Society of America under the terms of the OSA Open Access Publishing Agreement

OCIS codes: (000.1430) Biology and medicine; (170.3880) Medical and biological imaging; (170.1790) Confocal microscopy; (170.2520) Fluorescence microscopy; (170.4580) Optical diagnostics for medicine.

References and links

1. S. Weinbaum, J. M. Tarbell, and E. R. Damiano, "The structure and function of the endothelial glycocalyx layer," Annu. Rev. Biomed. Eng. **9**(1), 121–167 (2007).
2. A. N. Rizzo and S. M. Dudek, "Endothelial Glycocalyx Repair: Building a Wall to Protect the Lung during Sepsis," Am. J. Respir. Cell Mol. Biol. **56**(6), 687–688 (2017).
3. A. Burke-Gaffney and T. W. Evans, "Lest we forget the endothelial glycocalyx in sepsis," Crit. Care **16**(2), 121 (2012).
4. S. M. Haeger, Y. Yang, and E. P. Schmidt, "Heparan Sulfate in the Developing, Healthy, and Injured Lung," Am. J. Respir. Cell Mol. Biol. **55**(1), 5–11 (2016).
5. E. P. Schmidt, Y. Yang, W. J. Janssen, A. Gandjeva, M. J. Perez, L. Barthel, R. L. Zemans, J. C. Bowman, D. E. Koyanagi, Z. X. Yunt, L. P. Smith, S. S. Cheng, K. H. Overdier, K. R. Thompson, M. W. Geraci, I. S. Douglas, D. B. Pearse, and R. M. Tuder, "The pulmonary endothelial glycocalyx regulates neutrophil adhesion and lung injury during experimental sepsis," Nat. Med. **18**(8), 1217–1223 (2012).
6. X. Marechal, R. Favory, O. Joulin, D. Montaigne, S. Hassoun, B. Decoster, F. Zerimech, and R. Neviere, "Endothelial glycocalyx damage during endotoxemia coincides with microcirculatory dysfunction and vascular oxidative stress," Shock **29**(5), 572–576 (2008).
7. B. F. Becker, D. Chappell, D. Bruegger, T. Annecke, and M. Jacob, "Therapeutic strategies targeting the endothelial glycocalyx: acute deficits, but great potential," Cardiovasc. Res. **87**(2), 300–310 (2010).

#323318 https://doi.org/10.1364/BOE.9.002383
Journal © 2018 Received 20 Feb 2018; revised 16 Apr 2018; accepted 20 Apr 2018; published 26 Apr 2018

Biomedical Optics EXPRESS

8. E. P. Schmidt, K. H. Overdier, X. Sun, L. Lin, X. Liu, Y. Yang, L. A. Ammons, T. D. Hiller, M. A. Suflita, Y. Yu, Y. Chen, F. Zhang, C. Cothren Burlew, C. L. Edelstein, I. S. Douglas, and R. J. Linhardt, "Urinary Glycosaminoglycans Predict Outcomes in Septic Shock and Acute Respiratory Distress Syndrome," Am. J. Respir. Crit. Care Med. **194**(4), 439–449 (2016).
9. M. Sallisalmi, J. Tenhunen, R. Yang, N. Oksala, and V. Pettilä, "Vascular adhesion protein-1 and syndecan-1 in septic shock," Acta Anaesthesiol. Scand. **56**(3), 316–322 (2012).
10. J. Steppan, S. Hofer, B. Funke, T. Brenner, M. Henrich, E. Martin, J. Weitz, U. Hofmann, and M. A. Weigand, "Sepsis and major abdominal surgery lead to flaking of the endothelial glycocalix," J. Surg. Res. **165**(1), 136–141 (2011).
11. A. Nelson, I. Berkestedt, A. Schmidtchen, L. Ljunggren, and M. Bodelsson, "Increased levels of glycosaminoglycans during septic shock: relation to mortality and the antibacterial actions of plasma," Shock **30**(6), 623–627 (2008).
12. E. P. Schmidt, G. Li, L. Li, L. Fu, Y. Yang, K. H. Overdier, I. S. Douglas, and R. J. Linhardt, "The circulating glycosaminoglycan signature of respiratory failure in critically ill adults," J. Biol. Chem. **289**(12), 8194–8202 (2014).
13. D. R. Potter and E. R. Damiano, "The hydrodynamically relevant endothelial cell glycocalyx observed in vivo is absent in vitro," Circ. Res. **102**(7), 770–776 (2008).
14. H. Vink and B. R. Duling, "Identification of distinct luminal domains for macromolecules, erythrocytes, and leukocytes within mammalian capillaries," Circ. Res. **79**(3), 581–589 (1996).
15. T. W. Secomb, R. Hsu, and A. R. Pries, "Motion of red blood cells in a capillary with an endothelial surface layer: effect of flow velocity," Am. J. Physiol. Heart Circ. Physiol. **281**(2), H629–H636 (2001).
16. Y. Han, S. Weinbaum, J. A. E. Spaan, and H. Vink, "Large-deformation analysis of the elastic recoil of fibre layers in a Brinkman medium with application to the endothelial glycocalyx," J. Fluid Mech. **554**(-1), 217 (2006).
17. D. H. Lee, M. J. Dane, B. M. van den Berg, M. G. Boels, J. W. van Teeffelen, R. de Mutsert, M. den Heijer, F. R. Rosendaal, J. van der Vlag, A. J. van Zonneveld, H. Vink, and T. J. Rabelink; NEO study group, "Deeper penetration of erythrocytes into the endothelial glycocalyx is associated with impaired microvascular perfusion," PLoS One **9**(5), e96477 (2014).
18. J. W. VanTeeffelen, J. Brands, and H. Vink, "Agonist-induced impairment of glycocalyx exclusion properties: contribution to coronary effects of adenosine," Cardiovasc. Res. **87**(2), 311–319 (2010).
19. J. King, T. Hamil, J. Creighton, S. Wu, P. Bhat, F. McDonald, and T. Stevens, "Structural and functional characteristics of lung macro- and microvascular endothelial cell phenotypes," Microvasc. Res. **67**(2), 139–151 (2004).
20. A. P. Stevens, V. Hlady, and R. O. Dull, "Fluorescence correlation spectroscopy can probe albumin dynamics inside lung endothelial glycocalyx," Am. J. Physiol. Lung Cell. Mol. Physiol. **293**(2), L328–L335 (2007).
21. B. Afessa, B. Green, I. Delke, and K. Koch, "Systemic inflammatory response syndrome, organ failure, and outcome in critically ill obstetric patients treated in an ICU," Chest **120**(4), 1271–1277 (2001).
22. L. D. Hudson, J. A. Milberg, D. Anardi, and R. J. Maunder, "Clinical risks for development of the acute respiratory distress syndrome," Am. J. Respir. Crit. Care Med. **151**(2), 293–301 (1995).
23. P. Kim, M. Puoris'haag, D. Côté, C. P. Lin, and S. H. Yun, "In vivo confocal and multiphoton microendoscopy," J. Biomed. Opt. **13**(1), 010501 (2008).
24. K. Choe, Y. Hwang, H. Seo, and P. Kim, "In vivo high spatiotemporal resolution visualization of circulating T lymphocytes in high endothelial venules of lymph nodes," J. Biomed. Opt. **18**(3), 036005 (2013).
25. K. Choe, J. Y. Jang, I. Park, Y. Kim, S. Ahn, D. Y. Park, Y. K. Hong, K. Alitalo, G. Y. Koh, and P. Kim, "Intravital imaging of intestinal lacteals unveils lipid drainage through contractility," J. Clin. Invest. **125**(11), 4042–4052 (2015).
26. H. Seo, Y. Hwang, K. Choe, and P. Kim, "In vivo quantitation of injected circulating tumor cells from great saphenous vein based on video-rate confocal microscopy," Biomed. Opt. Express **6**(6), 2158–2167 (2015).
27. J. Ahn, K. Choe, T. Wang, Y. Hwang, E. Song, K. H. Kim, and P. Kim, "In vivo longitudinal cellular imaging of small intestine by side-view endomicroscopy," Biomed. Opt. Express **6**(10), 3963–3972 (2015).
28. Y. Hwang, J. Ahn, J. Mun, S. Bae, Y. U. Jeong, N. A. Vinokurov, and P. Kim, "In vivo analysis of THz wave irradiation induced acute inflammatory response in skin by laser-scanning confocal microscopy," Opt. Express **22**(10), 11465–11475 (2014).
29. D. Rittirsch, M. S. Huber-Lang, M. A. Flierl, and P. A. Ward, "Immunodesign of experimental sepsis by cecal ligation and puncture," Nat. Protoc. **4**(1), 31–36 (2009).
30. M. R. Looney, E. E. Thornton, D. Sen, W. J. Lamm, R. W. Glenny, and M. F. Krummel, "Stabilized imaging of immune surveillance in the mouse lung," Nat. Methods **8**(1), 91–96 (2011).
31. W. J. Lamm, S. L. Bernard, W. W. Wagner, Jr., and R. W. Glenny, "Intravital microscopic observations of 15-microm microspheres lodging in the pulmonary microcirculation," J. Appl. Physiol. **98**(6), 2242–2248 (2005).
32. K. Kim, K. Choe, I. Park, P. Kim, and Y. Park, "Holographic intravital microscopy for 2-D and 3-D imaging intact circulating blood cells in microcapillaries of live mice," Sci. Rep. **6**(1), 33084 (2016).
33. R. Skalak and P. I. Branemark, "Deformation of red blood cells in capillaries," Science **164**(3880), 717–719 (1969).
34. H. Noguchi and G. Gompper, "Shape transitions of fluid vesicles and red blood cells in capillary flows," Proc. Natl. Acad. Sci. U.S.A. **102**(40), 14159–14164 (2005).

Biomedical Optics EXPRESS

35. C. J. Zuurbier, C. Demirci, A. Koeman, H. Vink, and C. Ince, "Short-term hyperglycemia increases endothelial glycocalyx permeability and acutely decreases lineal density of capillaries with flowing red blood cells," J. Appl. Physiol. **99**(4), 1471–1476 (2005).
36. H. Vink and B. R. Duling, "Capillary endothelial surface layer selectively reduces plasma solute distribution volume," Am. J. Physiol. Heart Circ. Physiol. **278**(1), H285–H289 (2000).
37. M. Guizar-Sicairos, S. T. Thurman, and J. R. Fienup, "Efficient subpixel image registration algorithms," Opt. Lett. **33**(2), 156–158 (2008).
38. P. Kim, E. Chung, H. Yamashita, K. E. Hung, A. Mizoguchi, R. Kucherlapati, D. Fukumura, R. K. Jain, and S. H. Yun, "In vivo wide-area cellular imaging by side-view endomicroscopy," Nat. Methods **7**(4), 303–305 (2010).
39. G. Matute-Bello, G. Downey, B. B. Moore, S. D. Groshong, M. A. Matthay, A. S. Slutsky, W. M. Kuebler, and G. Acute Lung Injury in Animals Study Group, "An official American Thoracic Society workshop report: features and measurements of experimental acute lung injury in animals," Am. J. Respir. Cell Mol. Biol. **44**(5), 725–738 (2011).
40. K. Jung, P. Kim, F. Leuschner, R. Gorbatov, J. K. Kim, T. Ueno, M. Nahrendorf, and S. H. Yun, "Endoscopic time-lapse imaging of immune cells in infarcted mouse hearts," Circ. Res. **112**(6), 891–899 (2013).
41. A. D. Aguirre, C. Vinegoni, M. Sebas, and R. Weissleder, "Intravital imaging of cardiac function at the single-cell level," Proc. Natl. Acad. Sci. U.S.A. **111**(31), 11257–11262 (2014).
42. C. Vinegoni, S. Lee, R. Gorbatov, and R. Weissleder, "Motion compensation using a suctioning stabilizer for intravital microscopy," Intravital **1**(2), 115–121 (2012).
43. B. M. van den Berg, H. Vink, and J. A. Spaan, "The endothelial glycocalyx protects against myocardial edema," Circ. Res. **92**(6), 592–594 (2003).
44. S. Weinbaum, X. Zhang, Y. Han, H. Vink, and S. C. Cowin, "Mechanotransduction and flow across the endothelial glycocalyx," Proc. Natl. Acad. Sci. U.S.A. **100**(13), 7988–7995 (2003).
45. S. Reitsma, D. W. Slaaf, H. Vink, M. A. van Zandvoort, and M. G. oude Egbrink, "The endothelial glycocalyx: composition, functions, and visualization," Pflugers Arch. **454**(3), 345–359 (2007).
46. M. R. Looney and J. Bhattacharya, "Live imaging of the lung," Annu. Rev. Physiol. **76**(1), 431–445 (2014).
47. P. I. Johansson, J. Stensballe, L. S. Rasmussen, and S. R. Ostrowski, "High circulating adrenaline levels at admission predict increased mortality after trauma," J. Trauma Acute Care Surg. **72**(2), 428–436 (2012).
48. M. Rehm, D. Bruegger, F. Christ, P. Conzen, M. Thiel, M. Jacob, D. Chappell, M. Stoeckelhuber, U. Welsch, B. Reichart, K. Peter, and B. F. Becker, "Shedding of the endothelial glycocalyx in patients undergoing major vascular surgery with global and regional ischemia," Circulation **116**(17), 1896–1906 (2007).
49. S. Grundmann, K. Fink, L. Rabadzhieva, N. Bourgeois, T. Schwab, M. Moser, C. Bode, and H. J. Busch, "Perturbation of the endothelial glycocalyx in post cardiac arrest syndrome," Resuscitation **83**(6), 715–720 (2012).

1. Introduction

Endothelial surface layer (ESL) is an extracellular layer of the endothelial cells covering the luminal surface of the blood vessels, which consists of glycocalyx and bound plasma constituents [1, 2]. The ESL has been regarded as a barrier protecting the endothelial cell from circulating cells and large molecules, preventing platelet adherence and leukocyte adhesion. While being maintained as a membrane-bound structure in normal physiological condition, the ESL has been suggested to be degraded in systemic inflammatory condition including sepsis [3, 4]. Several studies have proposed inflammation-induced shedding of glycocalyx associated with endothelial dysfunction in inflammatory cascade [5–8]. Furthermore, recent clinical studies reported the elevation of glycocalyx constitution in the blood plasma and urine of human patients with sepsis, suggesting that the circulating glycocalyx fragment might be derived from the destruction of vascular ESL [8–12].

Although its importance as a marker of endothelial cell damage and impairment of vascular system, the visualization of ESL has remained as a challenging technical issue [1]. Due to its thin hydrated gel-like structure, ESL is easily degraded during fixation, and their thickness is underestimated in *ex vivo* study [13]. Recently, there have been several studies about the *in vivo* microscopic imaging of ESL utilizing the exclusion of circulating macromolecule dye from the ESL [5, 6]. The disadvantage of this approach is that it is relatively irrespective of the interaction between the glycocalyx and the actual circulating cells. Due to its elastic mechanical properties, the thickness of the endothelial glycocalyx is varying, dependent on flow and size of circulating cell inside the vessel [14, 15]. For example, during the leukocyte passage, glycocalyx is known to be temporarily degraded [16]. Meanwhile, glycocalyx is homogeneous and constant during the passage of erythrocyte [14,

Biomedical Optics EXPRESS

17, 18]. As a result, in consideration of the continuous interaction between glycocalyx and circulating erythrocyte [15], *in vivo* ESL analysis in the presence of sufficient erythrocyte flow is physiologically appropriate. If the limited access zone of erythrocyte inside the lumen of capillary could be identified with sufficient flow, the exclusion zone of red blood cell (RBC) can be regarded as physiologic ESL [14, 18]. From this point of view, pulmonary endothelium in the lung is reasonably ideal for investigating ESL *in vivo* as the lung is the organ with prevalent endothelial cell and the erythrocyte flow is massive and rapid enough to lift off the layer [1]. In addition, the thickness of ESL has been suggested to be more prominent in pulmonary capillary than the systemic vessel [5, 19, 20]. Furthermore, the lung is the most frequently failed organ during the progression of sepsis with the elevation of glycocalyx fragment in the blood [9–12], which suggests a potential role of pulmonary endothelial glycocalyx in endothelial dysfunction, vessel integrity, and organ failure [3, 21, 22].

To visualize and investigate pulmonary ESL *in vivo*, we utilized a custom-design video-rate laser scanning confocal microscope and a pulmonary imaging window chamber, which enabled a real-time subcellular-resolution imaging of the rapidly flowing erythrocyte *in vivo* [23–28]. With fluorescence angiography, the track of erythrocytes flowing in capillary was successfully visualized *in vivo*, which revealed the exclusion zone representing the pulmonary ESL. Finally, a sepsis-induced acute lung injury (ALI) model was utilized as an experimental model, and the degradation of pulmonary ESL was identified and evaluated *in vivo*.

2. Method

2.1 Animal modeling

Mice were housed and bred in an institutional animal facility in Korea Advanced Institute of Science and Technology (KAIST). C57BL/6N mice were purchased from OrientBio (Suwon, Korea) or bred in-house. Histone H2B-eGFP/β-actin-DsRed double-transgenic mouse was generated by cross-breeding Histone H2B-eGFP transgenic mouse (Stock No. 006069, Jackson Laboratory) and β-actin-DsRed transgenic mouse (kindly provided by Dr. Koh at KAIST). To induce sepsis-induced ALI mice model, high-grade cecal ligation and puncture (CLP) model was utilized according to the previously described method [29]. All animal experiments were performed in accordance with the standard guidelines for the care and use of laboratory animals and were approved by the Animal Care and Use Committee of KAIST (protocol no. KA2014-30). All surgeries were performed under anesthesia, and all efforts were made to minimize suffering.

2.2 Imaging system

To visualize the *in vivo* pulmonary microcirculation through the pulmonary imaging window, a custom-built video-rate laser-scanning confocal microscopy system was implemented as previously described [24–28]. Three laser modules with output wavelengths at 488 nm (MLD488, Cobolt), 561 nm (Jive, Cobolt), and 640 nm (MLD640, Cobolt) were used as excitation light sources. Using a rapidly rotating polygonal mirror with 36 facets (MC-5, aluminum coated, Lincoln Laser) for fast-axis scanning, a video-rate laser-scanning at 30Hz was achieved. Three photomultiplier tubes (PMT; R9110, Hamamatsu) with bandpass filters (FF02-525/50, FF01-600/37, FF01-685/40, Semrock) were used for multi-color fluorescence imaging. Using a three-channel frame grabber (Solios, Matrox) with sampling pixel rate of 10 MHz and a custom-written image acquisition software based on the Matrox Imaging Library (MIL9, Matrox), video-rate movies (30 Hz, 512 x 512 pixels) were recorded and displayed in real time.

Biomedical Optics EXPRESS

2.3 Intravital pulmonary imaging

Mice were anesthetized with Ketamine (80 mg/kg) and Xylazine (12 mg/kg). After anesthesia, intubation with 20 Gauge vascular catheter with the aid of illuminating guidewire was performed and connected to a mechanical ventilator (MouseVent, Kent Scientific). The anesthetized mice were ventilated with an inspiratory pressure of 24~30 mmHg, a respiratory rate of 120~130 breaths per minute, and a positive-end expiratory pressure of 2 cmH_2O. In addition, 2% isoflurane was delivered to maintain anesthesia status for the extended period. Pulse oximetry was applied to monitor oxygenation and survival status. The thermal probe was introduced into the rectum for continuous monitoring of body temperature. The body temperature of the mouse was maintained at 37.0 °C by using the homeothermic system (RightTemp, Kent Scientific). Tail vein was cannulated with a 30-gauge needle attached to the PE-10 tube for intravenous injection of molecular dye and cell. Mice were positioned in right lateral decubitus followed by dissection of left thoracotomy. Skin and muscle were dissected until the exposure of rib and then incision was made between 3rd and 4th rib to expose pleura. After thoracotomy, the pulmonary imaging window modified from the previously described studies [30, 31] to fit in our imaging system was applied to the surface of the pleura. The negative suction pressure of 20~30 mmHg provided by pump and regulator (NVC 2300a, EYELA) was applied via a tube connected to the imaging window. To visualize the vessel with a fluorescent dye, 400 μg (10 mg/ml) of fluorescein isothiocyanate (FITC) conjugated dextran dye (FD40, Molecular Weight 40 kDa, Sigma-Aldrich) was infused through the tail vein catheter right before the intravital imaging.

2.4 Imaging analysis

Ten areas of the subpleural vessel from each mouse satisfying enough flow of erythrocyte was selected, and the real-time movie was acquired at the speed of 30 frames per second with 512 x 512 pixels per frame. To improve contrast and signal-to-noise ratio, an averaged image was generated by using more than 30 frames with the frame-by-frame movement smaller than 3 pixels. To eliminate the motion-induced blur, image registration processing was performed for every frame by using a custom-written MATLAB (Mathworks) code. The gray value was acquired using a histogram function of ImageJ (NIH). As thresholds to find the RBC exclusion zone representing the ESL, the outline of FITC dextran fluorescence representing capillary lumen was defined as 75 percentiles of maximal gray value and outline of erythrocyte track was calculated from 50 percentiles of the sum of maximal and minimal gray value. For statistical analysis, all data were expressed as mean ± S.D., and comparison between groups was analyzed by *t-test*.

3. Results

3.1 Intravital real-time pulmonary imaging system

To image the lung in live anesthetized mice *in vivo*, we implemented a pulmonary imaging window device based on previously described design as shown in Fig. 1(a) [30, 31]. It was further modified to be integrated with the custom-built video-rate laser-scanning confocal microscopy platform [23–28]. The minimal negative suction pressure of 20~30 mmHg was applied via a suction tube to minimize the motion-induced interruption during the pulmonary imaging [30, 31]. To perform the direct pulmonary capillary imaging, the surgical procedure of thoracotomy was performed to expose the lung surface to the negative-pressurized suction chamber in the pulmonary imaging window. Intubation and mechanical ventilation with the ventilator were conducted to assist respiration during the pulmonary imaging, and homeostatic thermoregulation using the rectal temperature probe and heating pad were applied to prevent hypothermia induced by anesthesia and operative procedure as shown in Fig. 1(b). In addition, pulse oximetry was applied to monitor the oxygenation status and survival of mouse during the pulmonary imaging.

Biomedical Optics EXPRESS

3.2 In vivo cellular-level three-dimensional lung imaging

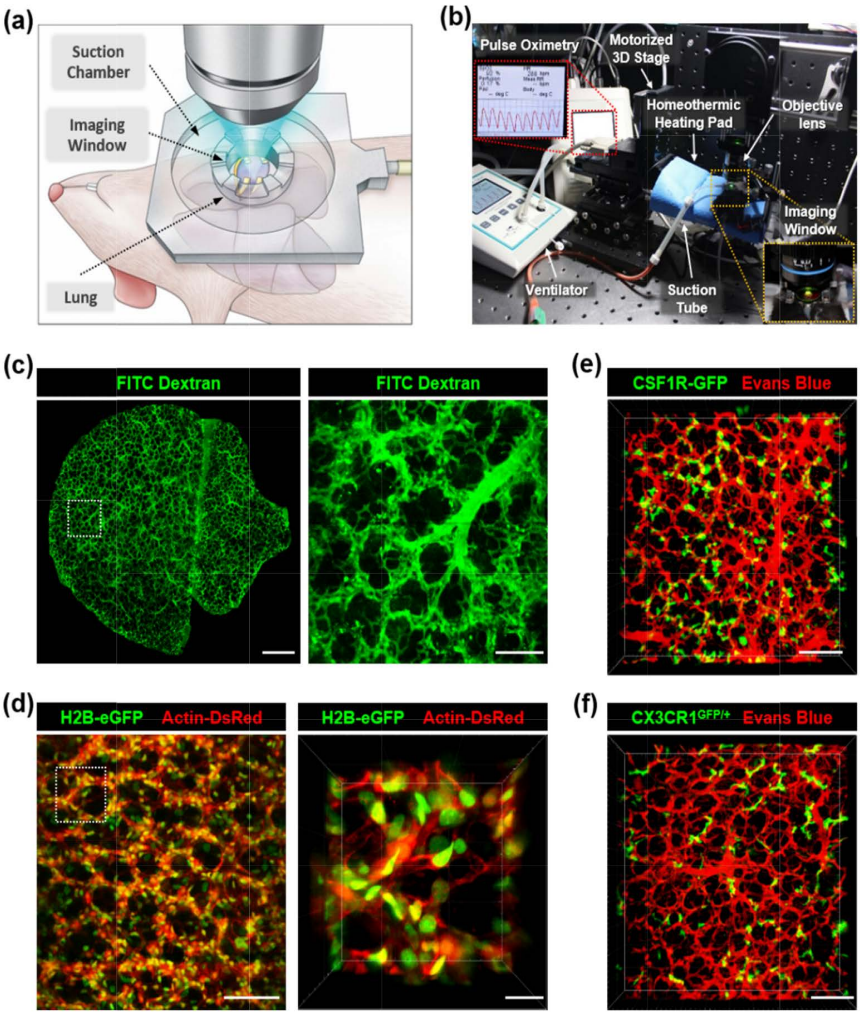

Fig. 1. *In vivo* cellular-level three-dimensional pulmonary imaging. (a) Schematic of the intravital pulmonary imaging including the micro-suction-based window. (b) Photograph of intravital pulmonary imaging setup consisted of a mechanical ventilator, pulse oximetry, animal stage, heating pad for body temperature regulation, and imaging window. (c) Wide-area mosaic and magnified image of the lung vasculature visualized by intravenously injected FITC dextran. Individual alveoli and capillary were clearly distinguished. Scale bars, 500 µm (mosaic), 100 µm (magnified). (d) Wide-area mosaic and subcellular level 3D intravital lung imaging of nucleus and cytoplasm of individual pulmonary cells in Histone H2B-eGFP/β-actin-DsRed double transgenic mouse (see also Visualization 2). Scale bars, 100 µm (mosaic), 10 µm (magnified). (e-f) Intravital pulmonary imaging of CSF1R-GFP cells representing alveolar macrophages and $CX3CR1^{GFP/+}$ cells representing mononuclear phagocytic cells. Blood vessels were visualized by intravenously injected TMR dextran. Scale bars, 100 µm.

Utilizing the intravital pulmonary imaging system, we have successfully achieved *in vivo* cellular-level 3D fluorescence imaging of lung in live mice. First, FITC-dextran with a molecular weight of 40 kDa was intravenously injected into a wildtype C57BL/6N mouse via tail vein as an agent for fluorescence angiography to visualize the vasculature of the lung *in vivo*. From the real-time movies acquired with the speed of 30 frames per second, individual

Biomedical Optics EXPRESS

flowing erythrocytes were clearly identified as dark spots inside the capillary lumen filled with the FITC-dextran (Visualization 1). By stitching multiple overlapping images obtained through the pulmonary imaging window, a wide-area mosaic image was constructed with high resolution enough to distinguish individual alveoli and capillary as shown in Fig. 1(c).

In addition, a genetically engineered histone H2B-GFP/β-actin-DsRed mouse model was used to demonstrate the capability of our imaging system to acquire multi-color subcellular resolution images as shown in Fig. 1(d) (Visualization 2). Individual cells expressing GFP exclusively in the nucleus and DsRed in both the cytoplasm and the nucleus could be clearly visualized *in vivo*, providing spatial information of individual cells and vasculature (Visualization 3). From the 3D rendered image with spots of H2B-GFP and surface of β-actin-DsRed, cell count represented by green spots and vessel volume represented by red surface could be quantified (Visualization 4). In the higher magnification view, high-resolution three-dimensional spatial information was attainable which could clarify the single cell location and relationship as shown in the right panel of Fig. 1(d) (Visualization 5). Furthermore, to demonstrate the feasibility of cellular visualization of immune surveillance behaviors, intravital three-dimensional pulmonary imaging was performed in transgenic mice including CSF1R-GFP [Fig. 1(e)] and $CX3CR1^{GFP/+}$ [Fig. 1(f)] representing macrophages and mononuclear phagocytic cells, respectively.

3.3 Real-time visualization of flowing erythrocyte and analysis of the exclusion zone inside capillary

As described above, utilizing the customized video-rate laser-scanning confocal microscopy platform [23–28], the real-time dynamics of the individual cell could be directly observed in the lung *in vivo*. In order to visualize the individual circulating cells in the pulmonary capillary those known to be mostly erythrocytes, negative staining of them based on the intravenous injection of fluorescent dye (FITC-dextran, 40 kDa) was facilitated as shown in Fig. 2(a) (Visualization 6). Individual erythrocytes with a parachute-like shape [32–34] could be clearly identified in the single frame obtained with the speed of 30 frames per second. While the intravenously injected 40 kDa of FITC-dextran fully filled up the lumen of capillary including the glycocalyx layer on the endothelial cell [35, 36], it was noticeable that the flowing erythrocytes did not directly contact the endothelial cell surface as shown in Fig. 2(b). Averaging of multiple frames with sub-pixel precision image registration algorithm [37, 38] was performed to generate an averaged image with improved signal to noise ratio (SNR) and contrast as shown in Fig. 2(c). It clearly revealed the track of multiple erythrocytes and the exclusion zone where circulating erythrocytes were precluded to infiltrate, which could be regarded as ESL [14, 18] protecting the endothelial cell from potential damage with frictional force inducible by direct contact with rapidly flowing erythrocyte as shown in Fig. 2(d).

Biomedical Optics EXPRESS

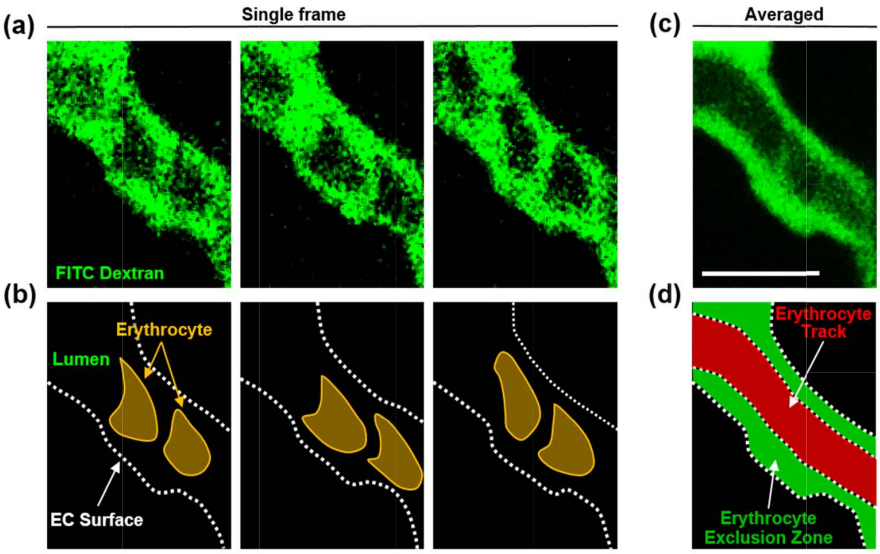

Fig. 2. Real-time imaging of circulating erythrocyte for visualization of exclusion zone inside the pulmonary capillary. (a-b) Representative real-time pulmonary capillary imaging with fluorescence angiography using intravenously injected FITC dextran. Individual circulating erythrocyte inside pulmonary capillary was identified in the single frame. (c-d) Averaged image highlight the track of flowing erythrocytes and its exclusion zone inside pulmonary capillary (see also Visualization 6). Scale bar, 10 µm.

3.4 Observation of endothelial surface layer degradation in a sepsis-induced lung injury

To further validate the exclusion zone as pulmonary ESL, its degradation in systemic inflammatory condition was investigated using cecal ligation and puncture (CLP) model which represent sepsis-induced lung injury [39]. 24 hours after the surgical procedure, a significantly reduced exclusion zone was confirmed in CLP model compared to the sham model, suggesting shedding of pulmonary ESL as shown in Fig. 3(a-b) (Visualization 7). Outermost line of FITC-dextran representing capillary lumen in the magnified images of Fig. 3(a) and 3(b) was delineated with a threshold of 75% of the maximal intensity in the exclusion zone. Erythrocyte track in capillary was delineated with a threshold of half-sum of the minimal intensity in erythrocyte track and the maximal intensity in the exclusion zone. As shown in the magnified image in Fig. 3(a-b), the thicknesses of exclusion zones were calculated as 1.76 µm and 1.17 µm in the sham model, 0.70 µm and 0.94 µm in CLP model. Capillary lumen and erythrocyte track identified by the described criteria and the intensity profile along the yellow dashed line are shown in Fig. 3(c-d). For quantitative statistical analysis, pulmonary capillary segments in 10 random spots of the lung from each mouse model were analyzed (3 mice per group). The width of endothelial surface layer of CLP group was much narrower than sham group (n = 30 per each group, mean ± S.D., 0.855 ± 0.337 µm vs. 1.614 ± 0.398 µm, $P < 0.001$, two-tailed t-test) while there was no significant difference in capillary diameter as shown in Fig. 3(e). This result is in accordance with previous observations of the pulmonary ESL [5]. In addition, to exclude the interference from the hydrodynamic effect, we measured the flowing velocity of erythrocyte inside the capillary. As shown in Fig. 3(g), no significant difference in velocity between two groups was identified.

Biomedical Optics EXPRESS

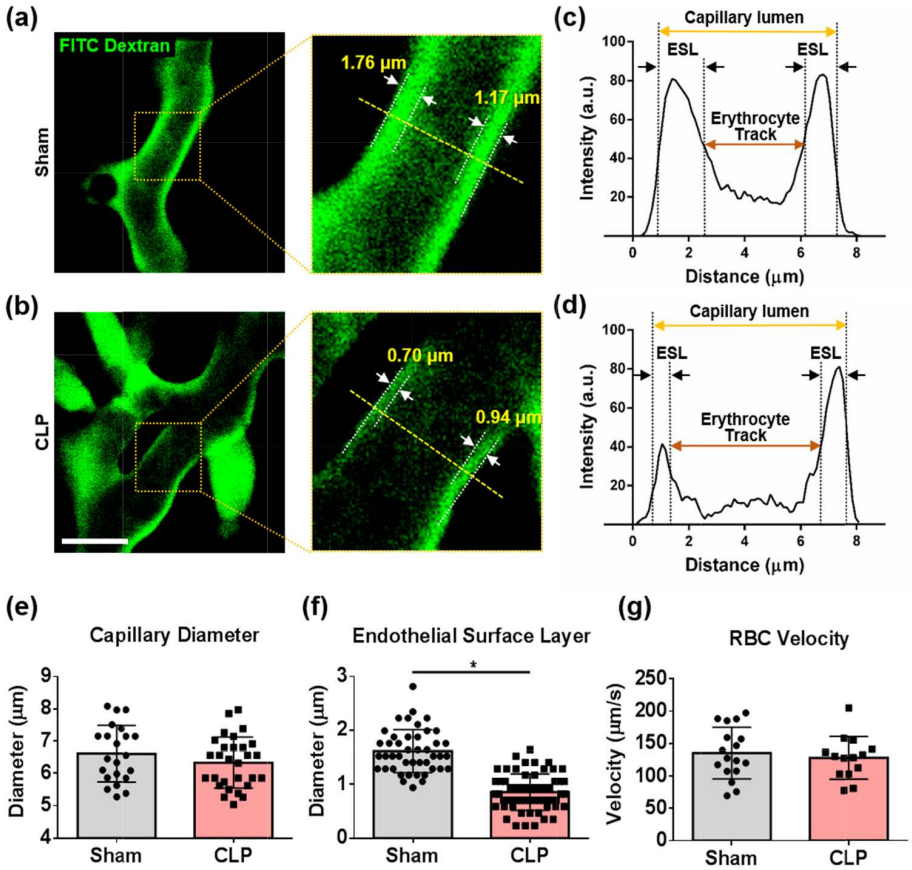

Fig. 3. In vivo imaging of endothelial surface layer degradation in a sepsis-induced lung injury model. (a-b) Representative image and magnified view of exclusion zone representing ESL in sham and CLP model (see also Visualization 7). (c-d) Identification of capillary lumen, erythrocyte, and ESL from fluorescence intensity profile along the yellow dashed line in (a) and (b), sham and CLP model, respectively. (e-g) Comparison of capillary diameter (n = 30 per group), ESL (n = 30 per group), and RBC velocity (n = 17 and 14, respectively) in sham and CLP model (Mean ± S.D., two-tailed t-test, *: $P < 0.001$). Scale bar, 10 μm.

4. Discussion

We achieved *in vivo* visualization of the dynamic pulmonary endothelial surface layer under the flow of erythrocytes by utilizing pulmonary imaging chamber combined with a custom-design video-rate laser scanning confocal microscopy. Suction-assisted tissue motion-stabilizing window allowed us to achieve a high quality real-time cellular-level imaging of pulmonary capillary. Individual circulating cells including erythrocyte, leukocyte, and other cells tagged with an endogenous fluorescent protein or exogenous fluorescent probe could be identified in the rapid flow of pulmonary microcirculation. Using fluorescence angiography and erythrocyte track analysis to identify exclusion zone analysis, we have successfully performed intravital imaging of pulmonary glycocalyx layer under a physiological condition with sufficient erythrocyte flow. It allowed us *in vivo* monitoring of pulmonary ESL which was degraded in systemic inflammatory status induced by cecal ligation and puncture.

Micro-suction has been utilized in various intravital microscopy study in cardiopulmonary research [30, 40–42]. It has been used to stabilize the organ during intravital microscopic imaging with minimal tissue damage and minimizing motion-induced artifact. There exist

concerns about potential tissue damage and interference of normal physiology of circulating cells in pulmonary microcirculation with the suction application. However, in accordance with previous studies, applying suction pressure of 20~30 mmHg has been reported to be generally safe for lung and heart [30, 40].

Consisted of heterogenic polysaccharide structure with glycoprotein, glycolipids, and glycosaminoglycan, its structure is easily degraded during perfusion and fixation [43]. Thereby, intravital visualization of the endothelial surface layer, glycocalyx, has been regarded as a long-term mission in vascular biology [1]. Recently, there have been several reports to visualize glycocalyx. Using distinct size-dependent permeability characteristics of glycocalyx to protect the endothelial cell from circulating macromolecules, two-color fluorescence angiography with dextran-fluorophore conjugates with different sizes was utilized to visualize the glycocalyx layer [6]. Another imaging study has been performed based on multi-mode differential interference contrast (DIC) imaging and fluorescence angiography, delineating blood vessel wall surface and lumen occupied by blood plasma, respectively [5]. The measurement of dynamic glycocalyx layer influenced by circulating cells including erythrocyte and leukocyte could be difficult [44, 45]. Our approach base on real-time erythrocyte imaging in pulmonary microcirculation facilitated a submicrometer-level dynamic visualization of pulmonary glycocalyx layer under interaction with circulating cell, erythrocyte.

The intravital visualization of glycocalyx using erythrocyte exclusion zone analysis was previously performed in cremasteric muscle [14, 36]. However, unlike peripheral microcirculation, *in vivo* visualization of endothelial glycocalyx layer in pulmonary microcirculation using erythrocyte exclusion zone imaging was technically challenging due to motion-artifact induced by respiration and difficulty in tracking individual erythrocytes in multiple interconnected capillary segments [46]. Rapid scanning using rotating polygonal mirror which enables real-time video-rate confocal fluorescent imaging to identify individual erythrocytes with negative-contrast could be a valid approach to mitigate difficulties described above, whereas most commercial confocal microscopy with the slower scanning device would suffer severe motion-artifact induced blurring. To our knowledge, this is the first intravital pulmonary ESL visualization using direct flowing erythrocyte exclusion zone analysis *in vivo*.

5. Conclusion

Our intravital imaging system successfully visualized pulmonary endothelial surface layer degradation followed by the loss of vessel integrity and organ failure, a characteristic of sepsis-induced acute lung injury (ALI). Further pathophysiology study and screening investigation of drug candidate of sepsis-induced ALI which targets ESL can be facilitated efficiently using our intravital imaging system. It can be a useful tool to investigate an impact of dynamic ESL changes in not only sepsis-induced lung injury but also various condition including major trauma [47], ischemia/reperfusion injury [48], and post-cardiac arrest syndrome [49] which affects pulmonary endothelial cell and vessel integrity.

Funding

Health Fellowship Foundation and the Global Ph.D. Fellowship Program (NRF-2015H1A2A1030717) through the National Research Foundation of Korea (NRF) funded by the Ministry of Education, Republic of Korea and the Global Frontier Project (NRF-2013M3A6A4044716); Basic Research Program (NRF-2017R1E1A1A01074190) funded by the Ministry of Science and ICT, Republic of Korea; Korea Healthcare Technology R&D Project (HI15C0399) funded by Ministry of Health and Welfare, Republic of Korea.

Biomedical Optics EXPRESS

Acknowledgements

The authors would like to thank Soyeon Ahn, Jieun Moon, Eunji Kong, Jingu Lee, Ryul Kim, Sujung Hong for advice and helpful discussion, Soo Yun Lee and Haeun Kim for their technical assistance.

Disclosure

The authors declare that there are no conflicts of interest related to this article.